Title

Giant Light-Emission Enhancement in Lead Halide Perovskites by Surface Oxygen Passivation

Journal

Nano Letters, 18(11)

ISSN

1530-6984

Authors

Lu, Dylan
Zhang, Ye
Lai, Minliang
et al.

Publication Date

2018-11-14

DOI

10.1021/acs.nanolett.8b02887

Peer reviewed

NANO LETTERS
Cite This: Nano Lett. 2018, 18, 6967−6973
Letter
pubs.acs.org/NanoLett

Giant Light-Emission Enhancement in Lead Halide Perovskites by Surface Oxygen Passivation

Dylan Lu,[†,‡] Ye Zhang,[†,‡] Minliang Lai,[†] Alex Lee,[†,‡] Chenlu Xie,[†] Jia Lin,[†,‡] Teng Lei,[†] Zhenni Lin,[‡,§] Christopher S. Kley,[†] Jianmei Huang,[†] Eran Rabani,[†] and Peidong Yang*[,†,‡,§,∥]

[†]Department of Chemistry, University of California, Berkeley, California 94720, United States
[‡]Materials Sciences Division, Lawrence Berkeley National Laboratory, Berkeley, California 94720, United States
[§]Department of Materials Science and Engineering, University of California, Berkeley, California 94720, United States
[∥]Kavli Energy NanoScience Institute, Berkeley, California 94720, United States

Supporting Information

ABSTRACT: Surface condition plays an important role in the optical performance of semiconductor materials. As new types of semiconductors, the emerging metal-halide perovskites are promising for next-generation optoelectronic devices. We discover significantly improved light-emission efficiencies in lead halide perovskites due to surface oxygen passivation. The enhancement manifests close to 3 orders of magnitude as the perovskite dimensions decrease to the nanoscale, improving external quantum efficiencies from <0.02% to over 12%. Along with about a 4-fold increase in spontaneous carrier recombination lifetimes, we show that oxygen exposure enhances light emission by reducing the nonradiative recombination channel. Supported by X-ray surface characterization and theoretical modeling, we propose that excess lead atoms on the perovskite surface create deep-level trap states that can be passivated by oxygen adsorption.

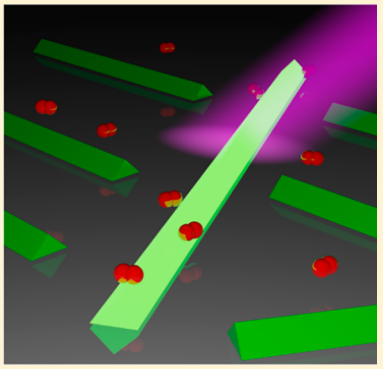

KEYWORDS: *Perovskites, surface passivation, photoluminescence, quantum efficiency, size effect*

The demand for high-efficiency energy conversion in solar energy harvesting and light-emitting devices has driven materials exploration and engineering with better functionality and performance.[1,2] Recently, metal-halide perovskites, crystalline materials with the typical form ABX_3, have emerged as a key building component for boosting current photovoltaic technologies.[3−5] The direct bandgap structures with tunable emission wavelengths also make metal-halide perovskites a good candidate for lasers and various light-emitting applications.[6−8] Compared with the organic counterparts, inorganic metal-halide perovskites have shown improved stability in moisture and heat with promising optical and electrical properties.[9,10] Such lead halide perovskites at the nanoscale provide a versatile platform for studying the dynamics of intrinsic material properties and for building spatially well confined light sources.[11−14] Despite the success of colloidal nanocrystals in achieving high quantum yields with surfactants,[11] solid-state halide perovskites without surface ligand engineering still have relatively low quantum efficiencies hindering their performance in photovoltaics and optoelectronic devices.[15−17] Besides, the light-emission quantum efficiency has barely been reported definitively for the intrinsic state of solid-state perovskites.[18,19]

Various chemical and physical approaches have been developed in order to improve the efficiency and performance of halide perovskites.[14,20−22] For example, postchemical treatment with pyridine activates originally dark grains in the perovskites by defect passivation at grain boundaries.[20] Heat induced phase transition in halide perovskites also helps reconfigure the crystal structure for higher emission efficiency.[14] Light soaking triggered lattice expansion in hybrid perovskite thin film solar cells leads to increased power conversion efficiency.[21] These efforts have brought attention to the importance of surface and lattice conditions that have long been generally investigated in semiconductor materials.[23,24] However, these approaches either lead to very limited improvement or involve significant changes in lattice structure, morphology, and emission properties, which may not be favorable in practical applications. The underlying mechanisms for enhancing efficiency also remain important open questions.

Here, we significantly improved the quantum efficiency in lead halide perovskites by oxygen gas exposure,[25−27] achieving close to 3 order-of-magnitude efficiency enhancement and about a 4-fold increase in the spontaneous carrier recombination lifetime as the dimension of perovskites shrank to the nanoscale. The morphology and size of halide perovskites were well controlled by further developed chemical vapor transport (CVT) growth method. Their intrinsic optical properties and response to gases were studied in-situ by controlled gas

Received: July 16, 2018
Revised: August 31, 2018
Published: September 28, 2018

DOI: 10.1021/acs.nanolett.8b02887
Nano Lett. 2018, 18, 6967−6973

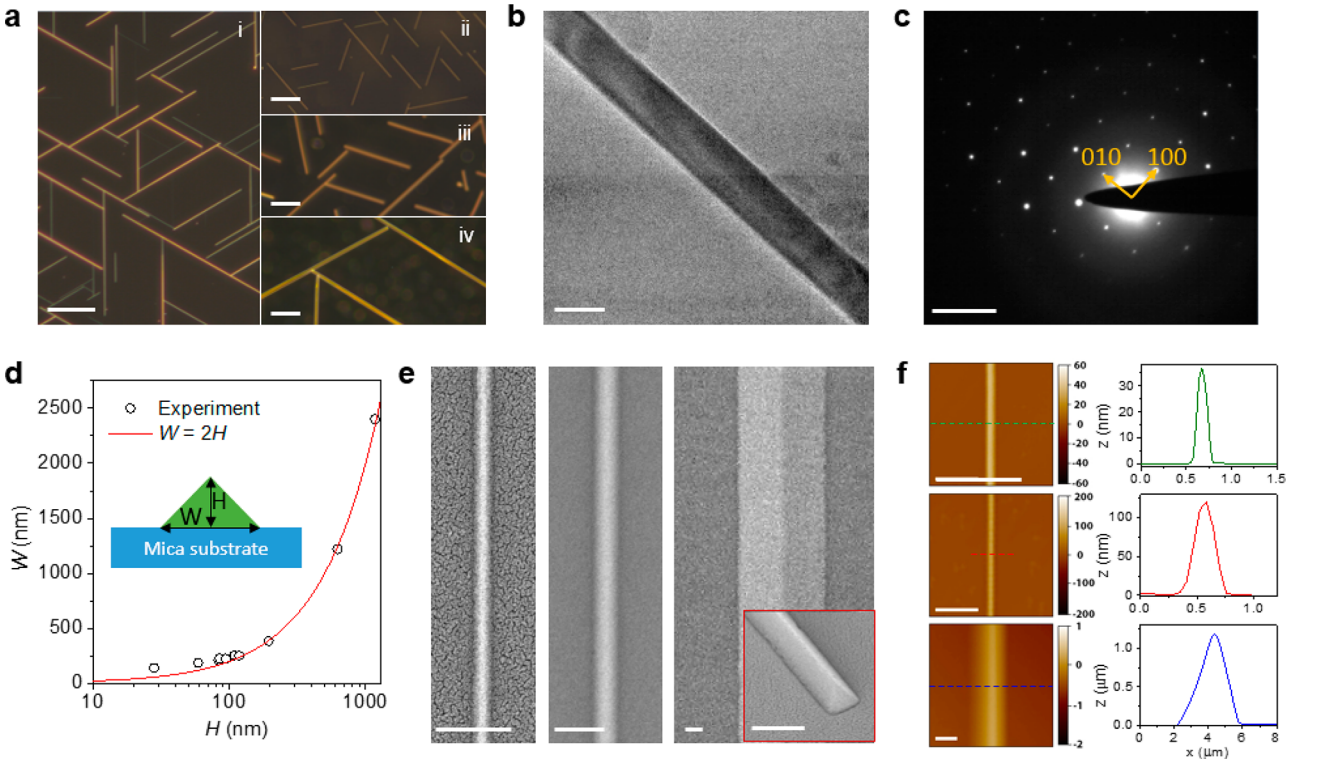

Figure 1. Single-crystal $CsPbBr_3$ nanowires grown by chemical vapor transport. (a) Optical dark field images of $CsPbBr_3$ nanowires grown on the mica substrates from different batches (i–iv) with lateral width from <200 nm (i,ii), ~1 μm (iii), to a few microns (iv). Scale bar, 50 μm. (b) TEM image of an individual nanowire. Scale bar, 100 nm. (c) SAED pattern from the nanowire in (b) with relevant crystallographic axes labeled. The zone axis is [001]. Scale bar, 5 nm^{-1}. (d) A mapping of the geometry structure for the width, W, and height, H (open black circles). Red line, $W = 2H$. Inset, a schematic drawing of the cross section of a nanowire on the mica substrate. (e) SEM images of individual nanowires with a lateral width of 141 nm, 248 nm, and 2.4 μm from left to right, respectively. Inset, a tilted SEM cross-sectional image of one nanowire. Scale bar, 500 nm. (f) AFM images of individual nanowires with a height of 36 nm, 116 nm, and 1.2 μm from top to bottom, respectively, with corresponding profiles along the dashed lines. Scale bar, 1 μm.

environment. Their emission quantum efficiency was further enhanced by reducing the perovskite diameter, rendering a linear dependence of enhancement factor on the surface-to-volume ratio. With theoretical modeling, we propose that lead-rich surface defects create trap states in the deep level, which dramatically quenches light emission. By passivating surface defects with oxygen adsorption, these trap states could be removed and therefore nonradiative recombination rate is greatly attenuated. This approach to enhance light emission was also generalized to halide perovskites of other compositions and dimensionalities prepared by different growth methods.

To probe the surface effect directly by noninvasive optical method, cesium lead halide perovskite single-crystalline nanowires were prepared by CVT epitaxial growth on mica substrates (see Methods for more details). The developed growth procedure allowed precise control of perovskite morphology and size by optimizing the substrate location, growth temperature, and growth time. Figure 1a shows the optical dark-field images of the cesium lead bromide ($CsPbBr_3$) nanowire ensemble horizontally aligned on the mica substrates with wide size coverages from less than 200 nm or around 1 μm to a few microns. The crystal structure of the nanowires was determined by selected area electron diffraction (SAED) in a transmission electron microscope (TEM) (Figure 1b,c). The SAED pattern confirms that the CVT grown nanowires are single-crystalline and can be indexed as the orthorhombic phase of $CsPbBr_3$. Single-crystalline phase is critical because it is resistant to interface and boundary defects as it appeared in polycrystalline and amorphous materials. The cross sections of individual $CsPbBr_3$ nanowires are in a triangular shape with the height H half of the width W, determined by correlated scanning electron microscopy (SEM) and atomic force microscopy (AFM) (Figure 1d–f). The height, H, was identified as the critical size in the following studies.

The optical properties and the dynamic response to a controlled gas environment were characterized in an in situ microscopic photoluminescence setup (Figure 2a, see Methods for more details). The material properties of as-made $CsPbBr_3$ nanowires were preserved by transferring fresh samples from the growth chamber into an Ar-gas-filled cell in a glovebox without exposing to external atmosphere prior to the measurement. Photoluminescence imaging of one nanowire shows highly contrasted green light emission before and after O_2 gas exposure (Figure 2b). Quantitative measurement by the corresponding photoluminescence spectra (Figure 2c) confirms a 197-fold enhancement in the emission efficiency from the original external quantum efficiency (EQE) of 0.06% to about 12.1% (see Methods for EQE measurement).

A systematic study was carried out for a collection of perovskites with size varying from about 30 nm to a few microns (Figure S1). The light-emission efficiency enhancement factor was found to be proportional to the surface-to-volume ratio, $1/H$ (Figure 2d). Compared with a change of less than 30-fold in bulk perovskites of a few micron size, close

DOI: 10.1021/acs.nanolett.8b02887
Nano Lett. 2018, 18, 6967–6973

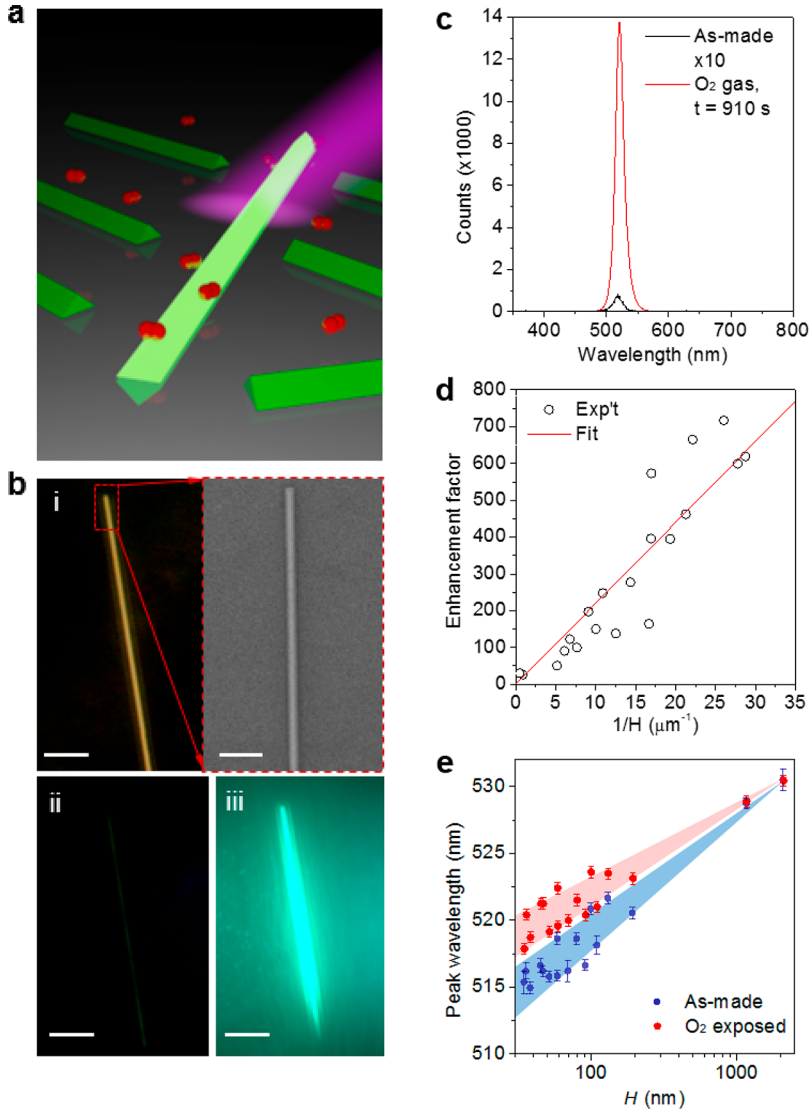

Figure 2. In situ microscopic photoluminescence characterization. (a) Schematic drawing of light-emission enhancement from lead halide perovskites after O_2 exposure, where the red objects represent O_2 molecules (not to scale). (b) Optical dark-field image of one $CsPbBr_3$ nanowire (i, scale bar, 10 μm) with a zoom-in SEM image (scale bar, 1 μm). Corresponding photoluminescence images for the nanowire before and after O_2 exposure are shown in (ii) and (iii), respectively (scale bar, 10 μm). The nanowire has a height of 109 nm, and a lateral width of 253 nm. (c) Photoluminescence spectra for the as-made $CsPbBr_3$ nanowire (black line) and that after O_2 exposure for 910 s (red line). The magnitude of black line has been multiplied by 10 for better comparison. (d) Photoluminescence enhancement factor plotted against $1/H$ for individual nanowires with sizes varying from ~30 nm to a few microns (open circles). A linear fitting curve is included in red line. (e) Peak emission wavelengths for individual as-made nanowires (in blue) and after O_2 exposure (in red). The error bar stands for standard deviation.

to an 800-fold emission efficiency enhancement was obtained for much smaller perovskites down to about 30 nm (Table S1), indicating the significant impact of the surface condition on the nanoscale perovskites. Lead halide perovskites at such a scale improved from extremely low intrinsic emission efficiencies of <0.02% to level with micron-scale perovskites at 12.4% after O_2 exposure. Besides well-preserved morphology, such O_2 exposure process had negligible impact on the emission features of the perovskites with minor peak emission redshift and small bandwidth reduction (Figure S2). The size-dependent peak emission wavelengths for the perovskites before and after the O_2 exposure show small but consistent redshifts (Figure 2e). Compared with the almost zero wavelength shift for micron-scale perovskites, a bigger redshift of about 5 nm occurred for nanoscale perovskites as the surface effect became dominant (Figure S3). The interaction of O_2 gas molecules with the perovskite surface may introduce distortion to the lattice structure and slightly close the bandgap by the presence of Urbach tails.[28]

In order to further identify the O_2 effect on the carrier recombination pathways, the carrier dynamics in halide perovskites was studied by in situ photoluminescence spontaneous recombination lifetime imaging (see Methods for more details). Figure 3a shows that the lifetime in a single $CsPbBr_3$ nanowire (i) gradually increases under O_2 exposure (ii–vi), consistent with the emission efficiency measurement. Quantitative fitting to spontaneous emission decay curves in the time domain identified a lifetime increase from 390 ps to 1.55 ns, resulting in about a 4-fold improvement (Figure 3b). Relatively uniform lifetime improvement was achieved on the nanowire by mapping out representative locations along the wire growth direction (Figure 3c). This behavior was observed

DOI: 10.1021/acs.nanolett.8b02887
Nano Lett. 2018, 18, 6967–6973

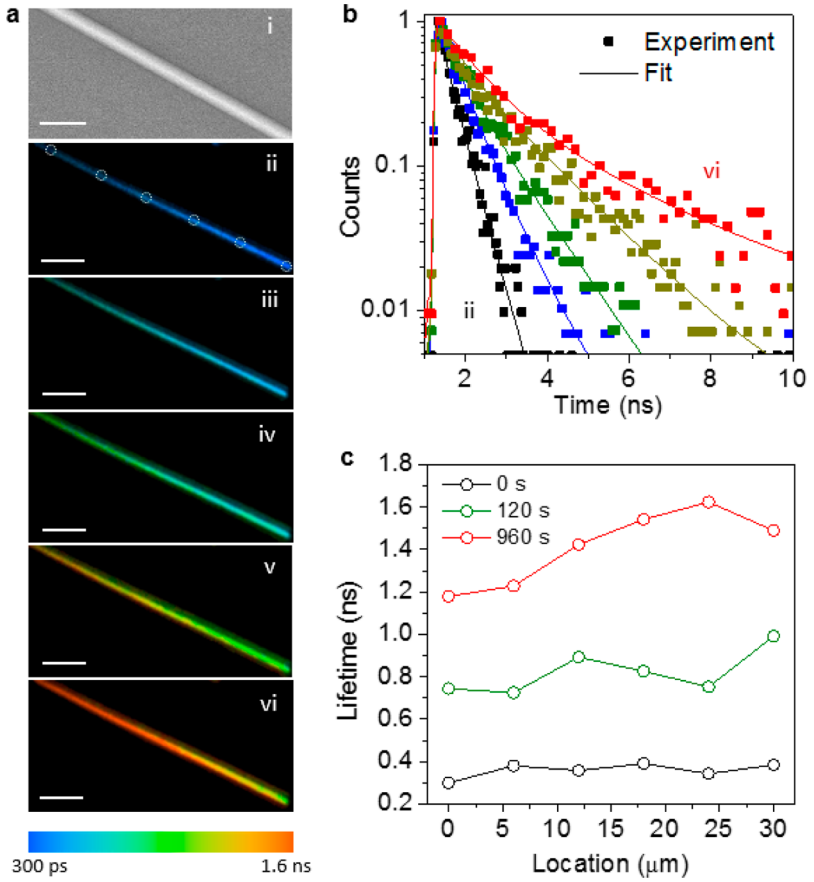

Figure 3. In situ time-resolved photoluminescence imaging. (a) SEM image of one $CsPbBr_3$ nanowire (i, scale bar, 1 μm) and corresponding photoluminescence lifetime images after O_2 exposure at t = 0 s (ii), 60 s (iii), 120 s (iv), 240 s (v), and 960 s (vi), respectively (scale bar, 5 μm). The nanowire has a thickness of 130 nm. (b) Time-resolved photoluminescence decay curves in square dots for the corresponding images in (a, ii–vi) at 18 μm from the right end of the nanowire and their fitting curves in solid lines. (c) Photoluminescence lifetime at different spatial locations of the individual nanowire with an even separation of 6 μm (dashed circles in (a, (ii)) at t = 0, 120, and 960 s, respectively.

in nearly all measurements on perovskites with different sizes (Figure S4). Further analysis indicates that the surface passivation by O_2 exposure improves the emission quantum efficiency and carrier recombination lifetime by effectively reducing the nonradiative recombination channel (see Supporting Information Section 1 for detailed analysis on the recombination channels).

Deeper insights into the microscopic mechanism of O_2 passivation were gained after ambient pressure X-ray photoelectron spectroscopy (AP-XPS) measurements were carried out to probe the surface structure of $CsPbBr_3$ (see Methods for more details). The XPS results suggest the existence of a Pb-rich condition on the surface of the as-made perovskites, which can be passivated by oxygen adsorption onto the Pb-rich surface defects (see Supporting Information Section 2 for detailed analysis on the XPS results).

To understand the role of surface defects on the spontaneous emission efficiency, we modeled the perovskite surface with two types of defect representing a stoichiometric excess of lead atoms on the surface (Figure 4a,b, see Supporting Information Section 3 for calculation details). For both types, a deep impurity level in the middle of the band gap was observed as a result of dangling bonds on the excess lead atoms (Figure 4c). Deep levels in the gap act as carrier traps, providing a pathway for undesired nonradiative recombination channels that lowers the quantum yields and reduces carrier lifetimes. After an oxygen molecule was introduced and adsorbed to the excess lead atoms on the surface, the deep levels were removed from the gap by saturating the dangling bonds (Figure 4c). These calculations illustrate a general mechanism where surface defects with excess lead are passivated by oxygen adsorption, removing trap states within the gap that lower the quantum efficiencies, consistent with experimental findings.

To quantify the time scale of emission enhancement by O_2 adsorption, time-dependent photoluminescence spectra and carrier recombination lifetime were captured for the dynamic process of individual $CsPbBr_3$ nanowires in O_2 gas (Figure S5). Integrated light-emission intensity dramatically increased within a few hundred seconds together with the recombination lifetime improvement. The dynamic process of strong light-emission enhancement could also be visualized by the in situ photoluminescence imaging at different time points, providing a spatially resolved evolution of light emission at the single nanostructure level (Figure S6). Such a fast optical response of perovskites to the O_2 gas facilitates practical applications and could be further controlled by different volumetric ratios of O_2 mixed with Ar gas (Figure S7). Higher O_2 concentration accelerated the increasing rate of integrated emission intensity that finally converged to similar levels. By switching to pure Ar gas, the enhanced photoluminescence could be mostly reversed by removing adsorbed oxygen, realizing light-emission control in perovskites (Figure S8). This reversible phenomen-

DOI: 10.1021/acs.nanolett.8b02887
Nano Lett. 2018, 18, 6967–6973

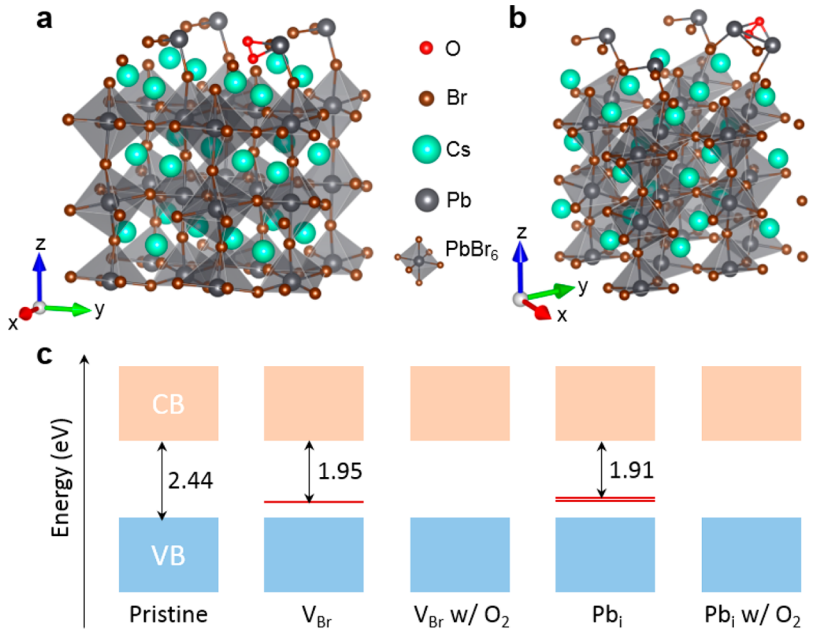

Figure 4. Theoretical modeling and energy level calculation. (a,b) Theoretical models of the perovskite surface as a 2D slab with crystal structures for the V_{Br} (a) and Pb_i (b) defect adsorbed by an O_2 molecule. V_{Br}, a bromine atom removed from the surface; Pb_i, an extra lead atom added to the surface. (c) Theoretical calculated energy levels around the band gap for various defect structures. Bandgaps are shown as the energy difference between the top of the valence band (VB) and the bottom of the conduction band (CB). The V_{Br} and Pb_i defects introduce occupied deep levels inside the band gap (red lines). In the case of Pb_i the defect levels are doubly degenerate. When O_2 is adsorbed onto the defect, the defect levels are removed.

on agrees well with the observation by AP-XPS (see Supporting Information Section 2).

Light-emission quantum efficiency improvement in solid-state perovskites by O_2 passivation was universally observed and generalized to different dimensionalities, material compositions, and sample preparation methods. Weak emission from the CVT grown $CsPbBr_3$ 2D nanoplate was enhanced after being exposed to O_2 gas (see Methods for growth details and Figure S9). Strong light-emission enhancement was also observed in perovskites with other halides including $CsPbCl_3$ and $CsPbI_3$ (see Methods for growth details, and Figures S10 and S11). In addition to CVT grown perovskites, lead halide perovskites prepared by the low-temperature solution process exhibited the same trend with enhanced emission intensity after O_2 passivation (see Methods for growth details and Figure S12). These demonstrations further highlight the importance of surface condition on the optical performance of lead halide perovskites, paving the way for mitigating surface imperfections in semiconductors.

In summary, giant light emission enhancement and lifetime elongation have been discovered in solid-state lead halide perovskites due to surface oxygen passivation. We find light emission quantum efficiencies enhanced by close to 3 orders of magnitude. The effect is dominated by surface to volume ratio and thus significant improvements are observed for nanoscale dimensions. The mechanism of such emission efficiency enhancement is not limited by dimensionalities, material compositions, and growth methods. Compared with emission efficiency improvement in colloidal quantum dots,[29] this study has focused on larger-scale nanomaterials without any surface ligand engineering. The initial EQE before oxygen passivation is relatively low compared with the original quantum efficiency of colloidal quantum dots. Besides, the defect sits in the deep level whereas most colloidal quantum dots have shallow electron traps.[29,30] By clarifying the general mechanism in solid-state halide perovskites, this study provides a guideline for achieving high-efficiency integrated optoelectronic devices.

METHODS

Growth of $CsPbX_3$. The $CsPbX_3$ ($X = Br^-$, Cl^-, I^-) perovskite nanowires were grown by the chemical vapor transport (CVT) method in a tube furnace (Thermolyne 79300). An alumina boat loaded with mixing precursors CsX (99.999% trace metals basis, Aldrich) and PbX_2 (99%, Aldrich) in a 1:1 molar ratio powder was placed at the heating center of a 1 in. diameter quartz tube. The freshly cleaved muscovite mica substrates (Grade V2, Ted Pella, Inc.) with (001) face exposed were placed in the downstream region of the tube. High purity N_2 (99.998%) as the carrying gas with a 200 sccm flowing rate was used to purge the whole tube system in order to eliminate oxygen and moisture in the tube before sample growth. In the growing process, the center temperature was set to ramp from room temperature to 550 °C with a heating rate of 50 °C/min (heating time ~10 min) and then was maintained at 550 °C for 5 to 10 min before cooling down to room temperature naturally. During the entire growth process, N_2 flow rate was set and stabilized at 100 sccm. After the growth was completed, the sample was taken out under N_2 protection and immediately transferred into the glovebox to eliminate exposure to air. The sample was placed inside an inert-gas filled cell in the inert atmosphere of the glovebox prior to the optical characterization. The size of the nanostructures was controlled by placing the mica substrate at different distances from the tube center. The growth parameter dependence on the specific distance and corresponding temperature is shown in Table S2. The $CsPbBr_3$ perovskite plates were also grown in the CVT tube furnace using the same growth conditions as the nanowire growth

DOI: 10.1021/acs.nanolett.8b02887
Nano Lett. 2018, 18, 6967−6973

except for the substrate position and growth time. The mica substrate should be placed at 16−18 cm (corresponding temperature: 410−460 °C) away from the tube center in order to get the 2D morphology. The furnace was maintained at 550 °C for 2 min.

The synthesis of $CsPbBr_3$ nanowires by low-temperature solution process was as follows. 460 mg PbI_2 (99.999%) was dissolved in 1 mL of anhydrous dimethylformide (DMF) and stirred at 70 °C overnight before further use. The PbI_2 solution was spun onto a PEDOT:PSS-coated glass substrates at 1000−3000 rpm for 120 s, then annealed at 100 °C for 15 min. The PbI_2 film was carefully submerged into a glass vial with 8 mg/mL CsBr (99.999%) solution in methanol (anhydrous, 99.8%), with the PbI_2 side facing up. The capped reaction vial was heated at 50 °C for 12 h. After cooling, the substrate was removed from the solution and washed twice in anhydrous isopropanol (each time for 30 s). The sample was then dried by heating to 50 °C for 5 min.

Structure Characterization of $CsPbX_3$. The morphology of $CsPbX_3$ was analyzed using a field-emission scanning electron microscope (FE-SEM, JEOL JSM-6340F). To acquire SEM images of nanowires on mica, the substrates were sputter coated with 5 nm gold using a Denton Vacuum Desk IV sputtering system. The thicknesses were measured by AAFM (MFP-3D Asylum Research, Oxford Instruments) equipped with an acoustic isolation chamber (AEK 2002) in noncontact mode at room temperature and inert atmosphere. Characterization of the lead halide perovskites by electron diffraction and TEM were conducted using an FEI Titan TEM operating at an accelerating voltage of 200 kV.

In Situ Microscopic Photoluminescence Measurement. The in situ microscopic photoluminescence characterization was carried out in a photoluminescence microscope system equipped with an in situ optical chamber (Instec, Inc., Figure S13). An excitation continuous-wave solid state laser at 375 nm (Coherent OBIS 375LX) was focused obliquely onto the perovskite sample in the chamber with a controlled power density (4.6 W/cm^2) by neutral density filters and a focused spot size. A laser filter (bandpass, 375 nm/6 nm) was used to clear the laser residual emission. A mechanical shutter was used to minimize the laser exposure to the sample. The photoluminescence from the perovskites was collected using a microscope objective (50×, numerical aperture = 0.55) before sending to the grating-based spectrograph (Princeton Instruments, SP-2300i) through an optical fiber for spectrum analysis. A long-pass emission filter at 390 nm was used to filter out laser signal. The spectrograph was equipped with a diffraction grating of 150 lines/mm (blaze wavelength at 300 nm) and coupled with a CCD detector with optimized detection efficiency by liquid nitrogen cooling to −120 °C. The acquisition time was controlled to be 0.1 s. The optical chamber was purged with O_2 or Ar gas (purity 99.995%, Praxair) using different valve-controlled tubes at a calibrated rate of 900 sccm. The spectra were taken every 30 s at the first 5 min and every 1 min afterward. The optical image was taken by a CCD camera (Zeiss AxioCam MRc 5).

The external quantum efficiency (EQE) of the perovskites was determined in the same system by comparing the emission to the absorption by the perovskites. The numerical aperture of the objective and absorption cross section of the perovskites were taken into account. The laser excitation was measured by illuminating the laser onto a reflective flat $BaSO_4$ coating. This measurement of EQE was also confirmed by EQE measurement in a photoluminescence system coupled with an integration sphere. The excitation at 375 nm was focused onto the sample with the spectra taken by the grating-based spectrograph. The ratio between the emission and the absorption by the perovskite sample determines the EQE.[31]

In Situ Photoluminescence Lifetime Imaging. The carrier recombination lifetime distribution of the perovskites at different gas environment were measured by a time-resolved photoluminescence microscopic imaging system coupled with an environmental chamber. A Ti:sapphire laser system (Spectra-Physics Mai Tai) with a pulse width of less than 100 fs and a repetition rate of 80 MHz was applied to excite the samples through a 50× objective with 0.6 numerical aperture at an excitation wavelength of 405 nm (second-harmonic laser wavelength). The illuminating power was controlled by the neutral density filter. The photoluminescence signal was collected by the same objective and filtered by a long-pass filter (488 nm) and a bandpass filter (530 nm/30 nm) before entering a controllable pinhole with a diameter of 50 μm in front of a Hamamatsu photomultiplier tube. The environmental chamber was purged with O_2 or Ar gas (99.995%, Praxair) using different valve-controlled tubes at a calibrated rate of 900 sccm. The lifetime images were taken every 30 s with a 25 s acquisition time.

In Situ X-ray Photoelectron Emission Spectroscopy Measurement. Ambient pressure X-ray photoelectron spectroscopy (AP-XPS) was performed at the Lawrence Berkeley National Laboratory Advanced Light Source (ALS) Beamline 9.3.2. A VG-Scienta R4000 HiPP analyzer was used. Samples were prepared on silicon substrates, and XPS spectra were collected using an incident X-ray energy of 630 eV. The atmosphere was controlled at UHV ($\sim 10^{-9}$ Torr) or by introducing Ar or O_2 gases into the chamber through different molecular leak valves. The binding energy for XPS spectra was calibrated with reference to the adventitious C 1s at 284.6 eV. A Shirley background was subtracted prior to analyzing the XPS spectra.

■ ASSOCIATED CONTENT

Supporting Information

The Supporting Information is available free of charge on the ACS Publications website at DOI: 10.1021/acs.nanolett.8b02887.

Detailed analysis on the carrier recombination channels, ambient pressure X-ray photoelectron spectroscopy, theoretical modeling and calculation, and supporting figures and tables (PDF)

■ AUTHOR INFORMATION

Corresponding Author

*E-mail: p_yang@berkeley.edu.

ORCID

Dylan Lu: 0000-0002-9238-2063
Chenlu Xie: 0000-0001-9215-6878
Teng Lei: 0000-0003-0356-1076
Peidong Yang: 0000-0003-4799-1684

Author Contributions

D.L. and Y.Z. contributed equally to this work. D.L. and P.Y. conceived the idea and designed the study. D.L. carried out the in situ optical characterizations with help from M.L. and J.L.. Y.Z., M.L., Z.L., and J.H. grew perovskite materials. Y.Z. and

DOI: 10.1021/acs.nanolett.8b02887
Nano Lett. 2018, 18, 6967−6973

C.S.K. performed the AFM measurements. T.L. performed the TEM characterization. C.X. performed the AP-XPS experiment. A.L. performed the molecular modeling with supervision from E.R.. D.L., A.L., E.R., and P.Y. wrote the manuscript with contributions from C.X., Y.Z., Z.L., and M.L. All authors discussed the results and revised the manuscript. P.Y. supervised the project.

Notes

The authors declare no competing financial interest.

■ ACKNOWLEDGMENTS

This work was supported by the U.S. Department of Energy, Office of Science, Office of Basic Energy Sciences, Materials Sciences and Engineering Division, under Contract No. DE-AC02-05-CH11231 within the Physical Chemistry of Inorganic Nanostructures Program (KC3103). The AP-XPS data was collected by the use of Beamline 9.3.2 at the Advanced Light Source, a DOE Office of Science User Facility under contract no. DE-AC02-05-CH11231. We acknowledge the help from E. J. Crumlin, Q. Kong, and H. Zhang for AP-XPS experiments. Photoluminescence lifetime imaging experiments were conducted at the CRL Molecular Imaging Center, supported by NSF DBI-0116016. We would like to thank H. Aaron and J.-Y. Lee for their help. D.L. would like to thank the Camille and Henry Dreyfus Foundation for funding, Award EP-14-151, and S. W. Eaton and L. Dou for help and discussion. Y.Z., M.L., C.X., and T.L. thank the fellowship support from Suzhou Industrial Park. C.S.K. acknowledges support by the Alexander von Humboldt Foundation.

■ REFERENCES

(1) Polman, A.; Knight, M.; Garnett, E. C.; Ehrler, B.; Sinke, W. C. *Science* **2016**, *352* (6283), aad4424.
(2) Stranks, S. D.; Snaith, H. *Nat. Nanotechnol.* **2015**, *10*, 391.
(3) Green, M. A.; Ho-Baillie, A.; Snaith, H. J. *Nat. Photonics* **2014**, *8* (7), 506−514.
(4) Lee, M. M.; Teuscher, J.; Miyasaka, T.; Murakami, T. N.; Snaith, H. *Science* **2012**, *338* (6107), 643−647.
(5) Zhou, H. P.; Chen, Q.; Li, G.; Luo, S.; Song, T. B.; Duan, H. S.; Hong, Z. R.; You, J. B.; Liu, Y. S.; Yang, Y. *Science* **2014**, *345* (6196), 542−546.
(6) Xing, G. C.; Mathews, N.; Lim, S. S.; Yantara, N.; Liu, X. F.; Sabba, D.; Gratzel, M.; Mhaisalkar, S.; Sum, T. C. *Nat. Mater.* **2014**, *13* (5), 476−480.
(7) Yuan, M. J.; Quan, L. N.; Comin, R.; Walters, G.; Sabatini, R.; Voznyy, O.; Hoogland, S.; Zhao, Y. B.; Beauregard, E. M.; Kanjanaboos, P.; et al. *Nat. Nanotechnol.* **2016**, *11* (10), 872−877.
(8) Kim, Y. H.; Cho, H.; Lee, T. W. *Proc. Natl. Acad. Sci. U. S. A.* **2016**, *113* (42), 11694−11702.
(9) Swarnkar, A.; Marshall, A. R.; Sanehira, E. M.; Chernomordik, B. D.; Moore, D. T.; Christians, J. A.; Chakrabarti, T.; Luther, J. M. *Science* **2016**, *354* (6308), 92−95.
(10) Liang, J.; Wang, C. X.; Wang, Y. R.; Xu, Z. R.; Lu, Z. P.; Ma, Y.; Zhu, H. F.; Hu, Y.; Xiao, C. C.; Yi, X.; et al. *J. Am. Chem. Soc.* **2016**, *138* (49), 15829−15832.
(11) Protesescu, L.; Yakunin, S.; Bodnarchuk, M. I.; Krieg, F.; Caputo, R.; Hendon, C. H.; Yang, R. X.; Walsh, A.; Kovalenko, M. V. *Nano Lett.* **2015**, *15* (6), 3692−3696.
(12) Zhu, H. M.; Fu, Y. P.; Meng, F.; Wu, X. X.; Gong, Z. Z.; Ding, Q.; Gustafsson, M. V.; Trinh, M. T.; Jin, S.; Zhu, X. Y. *Nat. Mater.* **2015**, *14* (6), 636−U115.
(13) Eaton, S. W.; Lai, M. L.; Gibson, N. A.; Wong, A. B.; Dou, L. T.; Ma, J.; Wang, L. W.; Leone, S. R.; Yang, P. D. *Proc. Natl. Acad. Sci. U. S. A.* **2016**, *113* (8), 1993−1998.
(14) Lai, M.; Kong, Q.; Bischak, C. G.; Yu, Y.; Dou, L.; Eaton, S. W.; Ginsberg, N. S.; Yang, P. *Nano Res.* **2017**, *10* (4), 1107−1114.
(15) Zhang, Q.; Ha, S. T.; Liu, X. F.; Sum, T. C.; Xiong, Q. H. *Nano Lett.* **2014**, *14* (10), 5995−6001.
(16) Marshall, K. P.; Walker, M.; Walton, R. I.; Hatton, R. A. *Nat. Energy* **2016**, *1*, 16178.
(17) Lin, J.; Lai, M.; Dou, L.; Kley, C. S.; Chen, H.; Peng, F.; Sun, J.; Lu, D.; Hawks, S. A.; Xie, C.; et al. *Nat. Mater.* **2018**, *17*, 261−267.
(18) Zhang, Q.; Su, R.; Liu, X. F.; Xing, J.; Sum, T. C.; Xiong, Q. H. *Adv. Funct. Mater.* **2016**, *26* (34), 6238−6245.
(19) Chen, J.; Fu, Y. P.; Samad, L.; Dang, L. N.; Zhao, Y. Z.; Shen, S. H.; Guo, L. J.; Jin, S. *Nano Lett.* **2017**, *17* (1), 460−466.
(20) deQuilettes, D. W.; Vorpahl, S. M.; Stranks, S. D.; Nagaoka, H.; Eperon, G. E.; Ziffer, M. E.; Snaith, H. J.; Ginger, D. S. *Science* **2015**, *348* (6235), 683−686.
(21) Tsai, H.; Asadpour, R.; Blancon, J. C.; Stoumpos, C. C.; Durand, O.; Strzalka, J. W.; Chen, B.; Verduzco, R.; Ajayan, P. M.; Tretiak, S.; et al. *Science* **2018**, *360* (6384), 67−70.
(22) Cho, H. C.; Jeong, S. H.; Park, M. H.; Kim, Y. H.; Wolf, C.; Lee, C. L.; Heo, J. H.; Sadhanala, A.; Myoung, N.; Yoo, S.; et al. *Science* **2015**, *350* (6265), 1222−1225.
(23) Williams, R. H. *Surf. Sci.* **1983**, *132* (1−3), 122−142.
(24) Wilmsen, C. W. *Physics and Chemistry of III-V Compound Semiconductor Interfaces*; Plenum Press: New York, 1985.
(25) Fang, H. H.; Adjokatse, S.; Wei, H. T.; Yang, J.; Blake, G. R.; Huang, J. S.; Even, J.; Loi, M. A. *Sci. Adv.* **2016**, *2* (7), e1600534.
(26) Galisteo-Lopez, J. F.; Anaya, M.; Calvo, M. E.; Miguez, H. *J. Phys. Chem. Lett.* **2015**, *6* (12), 2200−2205.
(27) Tian, Y. X.; Peter, M.; Unger, E.; Abdellah, M.; Zheng, K.; Pullerits, T.; Yartsev, A.; Sundstrom, V.; Scheblykin, I. G. *Phys. Chem. Chem. Phys.* **2015**, *17* (38), 24978−24987.
(28) Mocatta, D.; Cohen, G.; Schattner, J.; Millo, O.; Rabani, E.; Banin, U. *Science* **2011**, *332* (6025), 77−81.
(29) Koscher, B. A.; Swabeck, J. K.; Bronstein, N. D.; Alivisatos, A. P. *J. Am. Chem. Soc.* **2017**, *139* (19), 6566−6569.
(30) Kang, J.; Wang, L. W. *J. Phys. Chem. Lett.* **2017**, *8* (2), 489−493.
(31) Gargas, D. J.; Gao, H. W.; Wang, H. T.; Yang, P. D. *Nano Lett.* **2011**, *11* (9), 3792−3796.

DOI: 10.1021/acs.nanolett.8b02887
Nano Lett. 2018, 18, 6967−6973